A general model for analysis of acoustic phonons in piezoelectric super-lattices. Application to the (111)-AlAs/GaAs super-lattice



2007 J. Phys.: Condens. Matter 19 186209

(http://iopscience.iop.org/0953-8984/19/18/186209)

IOP PUBLISHING JOURNAL OF PHYSICS: CONDENSED MATTER

J. Phys.: Condens. Matter **19** (2007) 186209 (17pp) doi:10.1088/0953-8984/19/18/186209

# A general model for analysis of acoustic phonons in piezoelectric super-lattices. Application to the (111)-AlAs/GaAs super-lattice

**Victor Zhang**[1] **and Bahram Djafari-Rouhani**[2]

[1] IEMN-DOAE, Institut d'Electronique, de Microélectronique, et de Nanotechnologie, UMR CNRS 8520, Avenue Poincaré-BP 60069-59652 Villeneuve d'Ascq Cedex, France
[2] IEMN-DHS, Institut d'Electronique, de Microélectronique, et de Nanotechnologie, UMR CNRS 8520, Avenue Poincaré-BP 60069-59652 Villeneuve d'Ascq Cedex, France

E-mail: victor.zhang@iemn.univ-lille1.fr and bahram.djafari-rouhani@univ-lille1.fr

Received 18 December 2006, in final form 13 March 2007
Published 5 April 2007
Online at stacks.iop.org/JPhysCM/19/186209

**Abstract**

A general model is established for the analysis of acoustic phonons in an arbitrarily oriented piezoelectric super-lattice (SL). Analytical expressions are derived allowing the dispersion relation, transmission ($T$) and reflection ($R$) properties of the phonons to be numerically calculated for any incidence angle. Numerical investigation is exemplified for the (111) GaAs/AlAs SL with incidence in the $(\bar{1}10)$ plane. The obtained band structures confirm that the stop bands for both the shear horizontal and the coupled longitudinal and shear phonons appear inside the folded Brillouin zone, contrary to the (100) SL case in which they appear at the zone centre and edges. Both classical dispersion curves and Floquet slowness diagrams are used to present the edges of the Brillouin zones. Locations and widths of the stop bands inside the folded zones, as well as the $T$ and $R$ rates taking into account mode conversion, are studied as a function of frequency and incidence angle.

(Some figures in this article are in colour only in the electronic version)

## 1. Introduction

The physical phenomena related to acoustic phonons in both general one-dimensional multilayered elastic structures and 1D-*super-lattices* (SL) [1–11] have been the subject of intensive studies for several decades. A periodic SL has mechanical filtering effects on the propagation of high frequency acoustic phonons, and the basic transmission and reflection characteristics of phonons in such a structure are intimately related to the phonon dispersion relations. However, due to the complexity of the mathematics describing the acoustic propagation in anisotropic elastic media, most of the previous studies assumed the constituent

materials to be isotropic, and considered either only the *shear horizontal* (SH) mode or were limited to the normal incidence of phonons in order to be able to analytically tackle with the problem. Dispersion curves and the transmission rate of acoustic phonons in the (001) GaAs/AlAs SL are calculated for an arbitrary propagation direction using the continuum approximation with the elastic anisotropy included [3]. Both normal and oblique incidence of phonons in a GaAs/AlAs SL with a (111) interface have been investigated by Kato [6]. However, he studied the only SH mode, which is uncoupled from the other ones when the propagation is in the $(\bar{1}10)$ plane with a polarization in the $[\bar{1}10]$ direction parallel to the (111) interface. Some studies carried out very recently for 2D phononic crystals allow the inclusion materials to be anisotropic [12, 13] and/or piezoelectric [14, 15].

In this paper we present a general model allowing the analysis of phonon properties in an arbitrarily oriented piezoelectric SL. In particular, we extend Kato's study [6] to other modes of phonons in the same structural configuration. We point out immediately that we are interested here only in the acoustic phonons in piezoelectric materials within the framework of the quasi-static approximation, but not the optical ones as reported recently by some other researchers [16–18]. In section 2, we briefly recall some basic relations of the transfer matrix and *ordinary differential equation* (ODE) formalisms [19, 20] in order to introduce the field variables and to establish the general expressions for some important matrices that the subsequent development will need. Following this approach, valid for any layered structures with homogeneous planar layers, we first obtain, for a single layer and as a function of its state matrix, the local field solutions which automatically satisfy the field continuity conditions at layer interfaces. Section 3 is devoted to the phonon dispersion properties directly linked to the unit cell transfer matrix of the SL. Two forms of the dispersion relations will be presented for quasi *longitudinal* (L) and quasi *shear transverse* (T) polarized phonons, which are coupled to each other and with the electric field. Numerical examples are presented to illustrate the distinct characteristics of the coupled phonons as compared to the SH ones by considering a (111) GaAs/AlAs SL. We deduce in section 4 formal expressions of the transmission and reflection rates for the coupled phonons, taking into account the interaction and conversion between L and T modes. More numerical results are given in section 5 to show the specific dispersion and interaction properties of the coupled phonons. Conclusions are summarized in section 6.

## 2. ODE-based modelling and transfer matrix

A perfect SL is a 1D periodic structure with an infinite number of identical unit cells made of a finite number of layers each with finite thickness. A finite SL has a cell structure identical to the perfect SL but with a limited total length, i.e. the cell number is finite. A third form of SL structure is the semi-infinite SL, identical to a perfect SL except for the presence of a plane surface cutting the original SL into two parts; the surface can be either traction-free or in contact with a different medium. In this paper we are mainly concerned with the first two cases, though the modelling can be easily adapted to studying the third one with little modification. Figure 1 depicts the schematic of the SL structure that we consider in this paper. The unit cell of the periodic part consists of the GaAs and AlAs layers with a thickness of, respectively, $h_1$ and $h_2$; the substrate of the structure is assumed to be made of GaAs and the detector made of AlAs, both materials are (111)-oriented in the thickness direction, as in Kato [6].

However, these specifications are introduced only with regard to the numerical examples given to illustrate the model applications. Otherwise, the following analytical development is in fact equally valid for any multilayers constituted of arbitrarily oriented piezoelectric materials and arbitrary layer thicknesses. The material constants of each layer and substrate

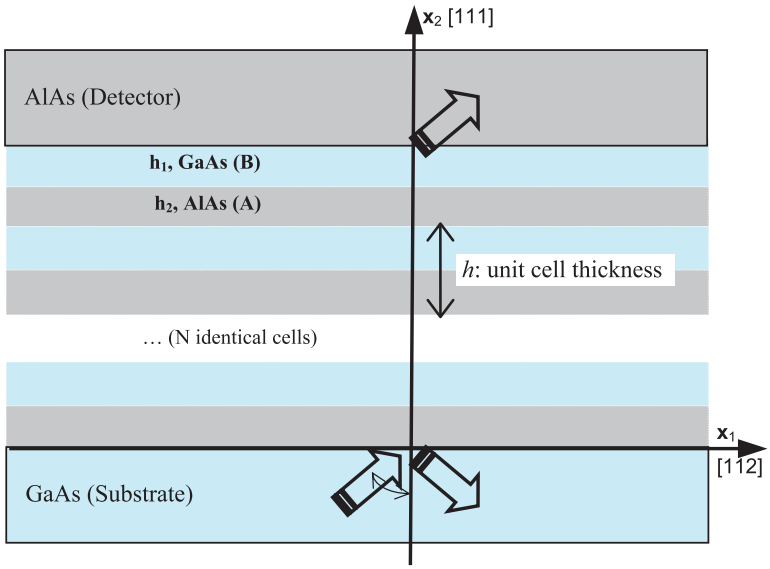


**Figure 1.** Schematic of the studied (111)-GaAs/AlAs super-lattice structure and the coordinate system used as well as the crystalline axes. The wide arrows symbolize the incident, reflected and transmitted waves.

are defined by its stiffness **c**, piezoelectric **e** and permittivity $\boldsymbol{\varepsilon}$ tensors and mass density $\rho$. In the working coordinate system $x_1x_2x_3$, we assume the incidence plane to be $x_1x_2$, or parallel to the $(\bar{1}10)$ plane in figure 1, and that all field quantities are uniform with $x_3$. The matrix form and numerical values of these tensors are given in the appendix for the SL configuration illustrated in figure 1. For a different orientations and/or materials, the **c**, **e** and $\boldsymbol{\varepsilon}$ tensors are required to be preliminarily transformed into the final working coordinates system by means of the Bond method, for example.

To maintain the generality, let us consider a plane wave (phonons) propagating in the $(x_1x_2)$ plane with an arbitrary polarization defined by a *generalized displacement vector* [21]

$$\mathbf{u} \equiv [u_1; u_2; u_3; \phi] \sim \mathbf{u}_0 \exp[\mathrm{j}\omega(t - s_1x_1 - s_2x_2)] \tag{1}$$

where $\mathrm{j} \equiv \sqrt{(-1)}$ and $s_i \equiv k_i/\omega$, **k** is the wavenumber vector, $\omega$ the angular frequency, and $s_i$ the slowness component in the $x_i$-direction. The subscript $i$ goes from 1 to 3. $\phi$ is the electrical potential. For convenience, we introduce a state vector $\boldsymbol{\tau}$ defined by $\boldsymbol{\tau} \equiv [T_{12}; T_{22}; T_{32}; D_2; v_1; v_2; v_3; \mathrm{j}\omega\phi]$, with $\mathbf{v} \equiv \partial\mathbf{u}/\partial t = \mathrm{j}\omega\mathbf{u}$. Herein and after, the *MATLAB Software* matrix notation[3] is adopted and a bold letter symbolizes either a vector or a matrix variable. $T_{i2}$ represent the components of the stress tensor normal to the layering, and $D_2$ is the electrical displacement along $x_2$. The so-defined vector $\boldsymbol{\tau}$ is continuous at each interface in the SL structure provided no metallization is present. Considered as an unknown function of $x_2$ for each layer, $\boldsymbol{\tau}$ is the solution of the following system of first-order vector-matrix ODE [19, 20]:

$$\frac{\mathrm{d}\boldsymbol{\tau}}{\mathrm{d}x_2} = (\mathrm{j}\omega)\mathbf{A}\boldsymbol{\tau}. \tag{2}$$

[3] For example, M(2:4, 1:3) means the matrix containing the 2nd to 4th rows of M and the 1st to 3rd columns of M; M(2:4,:) means the same row selection of M but all the columns of M, and a new row is indicated by a semicolon.

The local state matrix $\mathbf{A}(8 \times 8)$ in (2) is of the form

$$\mathbf{A} = \begin{bmatrix} \mathbf{G}_{12}\mathbf{G}_{22}^{-1}s_1 & \left(\mathbf{G}_{12}\mathbf{G}_{22}^{-1}\mathbf{G}_{21} - \mathbf{G}_{11}\right)s_1^2 + \boldsymbol{\rho}_0 \\ \mathbf{G}_{22}^{-1} & \mathbf{G}_{22}^{-1}\mathbf{G}_{21}s_1 \end{bmatrix}. \tag{3a}$$

In (3*a*), $\boldsymbol{\rho}_0$ is a $4 \times 4$ matrix of which all elements are zero except the first three main diagonal ones, which are equal to the mass density $\rho$, and the $4 \times 4$ matrices $\mathbf{G}_{jl}$ are given in terms of the material constants by

$$\mathbf{G}_{jl} = \begin{bmatrix} c_{1j1l} & c_{1j2l} & c_{1j3l} & e_{l1j} \\ c_{2j1l} & c_{2j2l} & c_{2j3l} & e_{l2j} \\ c_{3j1l} & c_{3j2l} & c_{3j3l} & e_{l3j} \\ e_{j1l} & e_{j2l} & e_{j3l} & -\varepsilon_{jl} \end{bmatrix}, \qquad j, l = 1, 2, 3. \tag{3b}$$

In addition to the material and orientation of the relevant layer, the state matrix $\mathbf{A}$ depends on the $x_1$-slowness ($s_1$), or the incidence angle, but it is independent of the frequency. This is due to the form we are using for the state vector, which is different from the one used in Braga and Herrmann [22].

The general solution of the ODE system (2), well known from linear system theory, can be written out as a linear combination of the modal solutions [20]:

$$\boldsymbol{\tau}(x_1, x_2, t) = \mathbf{Q}\mathbf{E}(x_2)\mathbf{y}\mathrm{e}^{\mathrm{j}\omega(t - s_1 x_1)} \tag{4}$$

where $\mathbf{E}(x_2) \equiv \mathrm{e}^{-\mathrm{j}\omega \mathbf{s}_2 x_2}$, with $\mathbf{s}_2$ being a diagonal matrix, we call it the *spectral matrix*, constructed with the elements $s_2^{(m)}$ ($m$ = 1–8), and $\mathbf{Q} \equiv [\ldots, \mathbf{Q}^{(m)}, \ldots]$ is an eight-dimensional *modal matrix*. Here, $-\mathrm{j}\omega s_2^{(m)} \equiv \lambda^{(m)}$ is the $m$th eigenvalue of the matrix $[\mathrm{j}\omega\mathbf{A}]$, and $\mathbf{Q}^{(m)}$ is the $\lambda^{(m)}$-associated eigenvector, determined with a certain norm. Finally, $\mathbf{y} \equiv [\ldots; y^{(m)}; \ldots]$ is the modal amplitude vector to be specified by the boundary conditions. All these quantities are implicit functions of $s_1$ and of the material constants. To be definite, we assume throughout the paper that the incident modes are numbered 1–4 and the reflected modes 5–8. Thus $m = 1, 2, 3$ and 4 refer to the EM (electromagnetic), L, T and SH acoustic modes, and $m = 8, 7, 6$ and 5 to the corresponding reflected ones, respectively. The form of the solution in (4) applies to any layer when using the appropriate material constants, i.e. the relevant eigenvalues and eigenvectors. In particular, at the top ($x_2 = H_n$) and bottom ($x_2 = H_n - h_n$) surfaces of the $n$th layer, it reads

$$\boldsymbol{\tau}_n^+ \equiv \boldsymbol{\tau}_n(x_2 = H_n) = \mathbf{Q}_n\tilde{\mathbf{y}}_n^+ \tag{5a}$$

and

$$\boldsymbol{\tau}_n^- \equiv \boldsymbol{\tau}_n(x_2 = H_n - h_n) = \mathbf{Q}_n\tilde{\mathbf{y}}_n^- \tag{5b}$$

with $\tilde{\mathbf{y}}_n^{\pm} \equiv \mathbf{E}_n^{\pm}\mathbf{y}_n$, $\mathbf{E}_n^+ \equiv \mathbf{E}_n(x_2 = H_n)$, and $\mathbf{E}_n^- \equiv \mathbf{E}_n(x_2 = H_n - h_n)$. Herein and after, the common scalar factor $\exp[\mathrm{j}\omega(t - s_1 x_1)]$ is omitted except when it is necessary. Eliminating from (5*a*), (5*b*) the common amplitude $\mathbf{y}_n$ yields a relation between $\boldsymbol{\tau}_n^+$ and $\boldsymbol{\tau}_n^-$

$$\boldsymbol{\tau}_n^+ = \mathbf{P}_n\boldsymbol{\tau}_n^- \tag{6}$$

via the *layer transfer matrix* $\mathbf{P}_n$ which, expressed in terms of the modal matrix, is of the form

$$\mathbf{P}_n \equiv \mathbf{Q}_n\mathbf{E}_n^0\mathbf{Q}_n^{-1}, \tag{7}$$

where $\mathbf{E}_n^0 \equiv \mathrm{e}^{-\mathrm{j}\omega \mathbf{s}_2 h_n}$ is the so-called propagator, with $\mathbf{s}_2$ denoting the spectral matrix of the layer $n$.

### 3. Floquet dispersion relation and slowness surfaces

We begin by considering an infinite periodic SL having the unit cell transfer matrix $\mathbf{P}_c$. For an arbitrarily anisotropic structure exhibiting a spatial periodicity in one direction, Floquet theory is perhaps the most appropriate tool to model the behaviour of the phonons. The dispersion relation of the phonons in a SL is uniquely deduced from the eigenvalues of $\mathbf{P}_c$. According to the Floquet theorem, dynamic variables at any coordinate $x_2$ in a periodic medium of period $h$ are related to those at $x_2 + h$ by [22, 23]

$$\boldsymbol{\tau}(x_2 + h) = \mathrm{e}^{-\mathrm{j}k_f h}\boldsymbol{\tau}(x_2). \tag{8}$$

$k_f$ in (8) is the yet unknown SL wavenumber, or the *Floquet wavenumber*. When applied at the boundaries of the first unit cell ($x_2 = 0$), (8) gives $\boldsymbol{\tau}(h) = \mathrm{e}^{-\mathrm{j}k_f h}\boldsymbol{\tau}(0)$. On the other hand, applying the transfer matrix relation (6) to the same cell yields $\boldsymbol{\tau}_2^+ = \mathbf{P}_c\boldsymbol{\tau}_1^-$. Then, by equating the right-hand sides of these two relations and noting $\boldsymbol{\tau}_2^+ \equiv \boldsymbol{\tau}(h)$ and $\boldsymbol{\tau}_1^- \equiv \boldsymbol{\tau}(0)$, we obtain

$$(\mathbf{P}_c - \lambda_f\mathbf{I})\boldsymbol{\tau}(0) = \mathbf{0} \qquad \text{with } \lambda_f \equiv \mathrm{e}^{-\mathrm{j}k_f h} \tag{9a}$$

and $\mathbf{I}$ is a $8 \times 8$ identity matrix. Equation (9*a*) has eight eigenvalues $\lambda_f^{(m)}$, ($m = 1$–8), which are the roots of the characteristic equation

$$\det(\mathbf{P}_c - \lambda_f\mathbf{I}) = 0. \tag{9b}$$

To analyse the relationship between the eigenvalues and properties of the Floquet waves, we write

$$\lambda_f \equiv \rho\mathrm{e}^{-\mathrm{j}\Theta} = \rho\mathrm{e}^{-\mathrm{j}\theta}, \tag{10a}$$

where $\rho$ and $\Theta$ are the modulus and argument of $\lambda_f$. Identification of $\lambda_f$ from (9*a*) and (10*a*) yields

$$k_f h = \mathrm{j}\ln(\rho) + (\theta + M2\pi), \tag{10b}$$

where $M$ is an integer such that $-\pi < \theta \leqslant \pi$. The eight associated Floquet wavenumbers $k_f^{(m)}$ and eigenvectors $\boldsymbol{\tau}_f^{(m)}$ ($m = 1$–8) determined from (9*a*) and (9*b*) define what are called Floquet waves. They can propagate independently in an unbounded periodic medium (i.e. a perfectly periodic SL), but they must be coupled together when boundaries or some foreign (defect) layers are present [22]. The $m$th Floquet wave has a polarization given by $\boldsymbol{\tau}_f^{(m)}$ and a velocity related to $k_f^{(m)}$. It consists of a combination of classical plane bulk modes in the homogeneous layers and represents the net wave motion after multiple reflections and refractions through the layering. When $k_f^{(m)}$ is real, which requires $\rho = 1$, the Floquet wave (mode $m$) is propagating. The corresponding frequencies are then in the pass bands. For $\rho \neq 1$, $k_f^{(m)}$ is complex, or purely imaginary if $\theta = 0$. The corresponding Floquet wave cannot propagate in the relevant frequency bands, which are named stop bands or frequency gaps. As a result, a periodically layered structure can behave as a mechanical filter. The choice of the Brillouin branch, i.e. the integer $m$, does not affect the general solution since both the polarization and velocity of a Floquet wave only depend on $\lambda_f$, namely the values of $\rho$ and $\theta$. This indeterminacy in the real part of the Floquet wavenumber is a characteristic of waves propagating in the periodic structures. We would also like to point out that the determinant of $\mathbf{P}_c$ is not always equal to 1 except for $s_1 = 0$ (normal incidence), though its modulus is always unity for any $s_1$ value. If $\mathrm{Im}(\det[\mathbf{P}_c]) \neq 0$, at least two eigenvalues, say $\lambda_f^{(\nu)}$, have unit magnitude. In this case, $k_f^{(\nu)}$ is real and, for an anisotropic configuration, $1/\lambda_f^{(\nu)}$ is not necessarily an eigenvalue of the matrix $\mathbf{P}_c$ even if $\lambda_f^{(\nu)}$ is. This stems from the fact that the angles of incidence and reflection are not the same [6, 22]. As a general rule, the eigenvalues of $\mathbf{P}_c$ are 'either of unit magnitude or else occur in pairs such that one is the complex conjugate of the reciprocal of the other' [22].

Degeneracy occurs when $\lambda_{\mathrm{f}}^{(m)} = \pm 1$, i.e. $\rho = 1$ and $\theta = 0$ or $\pi$, or equivalently $k_{\mathrm{f}}^{(m)} h = 2M\pi$ or $(2M + 1)\pi$. This happens when the $m$th Floquet wave propagates parallel to the layering and remains standing in the normal direction.

Knowing the Floquet wavenumbers, we can by analogy with the classical plane waves draw Floquet slowness curves by defining

$$s_f^{(m)} \equiv k_f^{(m)}/\omega, \qquad m = 1\text{–}8 \tag{10c}$$

$s_{\mathrm{f}}^{(m)}$ is considered as the Floquet slowness of the $m$th mode. We can write (10*b*) with $M = 0$

$$s_{\mathrm{f}}^{(m)} = [\mathrm{j}\ln(\rho) + \theta]/\omega h. \tag{10d}$$

A real $s_{\mathrm{f}}^{(m)}$ means a propagating mode (the corresponding frequencies are situated in a pass band), and a complex or purely imaginary $s_{\mathrm{f}}^{(m)}$ an evanescent mode (frequencies in a stop band). The most remarkable feature of the dispersion spectrum of waves in the periodic structures, i.e. the existence of the stop bands (or gaps) and pass bands of frequency, can be observed from two different forms of the dispersion relations. Floquet wavenumbers plotted against frequency for a given incidence angle pertain to the dispersion relations ($k_{\mathrm{f}} - \omega$, $|s_1)$, while wavenumbers as a function of the incidence angle for a fixed frequency permit us to draw the slowness curve diagrams that we call dispersion surfaces ($s_{\mathrm{f}} - s_1$, $|\omega$).

Now, we take for numerical investigations the same configuration as studied by Kato [6] but we aim to analyse the L and T phonons in addition to the SH ones. The values of $h_1$ and $h_2$ are assumed to be 19.56 and 48.9 nm, respectively, the cell thickness ($h = h_1 + h_2$) thus equals 68.46 nm, cf figure 1. Let $\mathbf{P}_{\mathrm{c}} = \mathbf{P}_{\mathrm{B}}\mathbf{P}_{\mathrm{A}}$ be the unit cell matrix, where $\mathbf{P}_{\mathrm{A}}$ and $\mathbf{P}_{\mathrm{B}}$ denote the transfer matrix of the layers with odd (AlAs) and even (GaAs) number, respectively. They are computed from (7) by using the appropriate modal ($\mathbf{Q}$) and spectral ($\mathbf{s}_2$) matrices and $h_n$. Figure 2(a) shows the dispersion curves of the SH phonons, together with the small imaginary part in the stop bands of the Floquet wavenumbers $k_{\mathrm{f}}$. They were calculated for an oblique incidence of 15° from the [111] direction. The position of the stop bands $k_{\mathrm{B}}$ for the SH phonons was determined in closed form in [6], and the locations of the points ($k_{\mathrm{B}}$, $\omega_{\mathrm{B}}$) in $k_{\mathrm{f}} - \omega$ space are on some straight lines ($L_1$, $L_2$) with a given slope, this means that $k_{\mathrm{B}}$ is directly proportional to the Bragg frequency $\omega_{\mathrm{B}}$ (see figure 2(a)). The dispersion curves of the L and T phonons are plotted in figures 2(c) and (d). They confirm that, in oblique incidence, the stop bands of the L and T phonons, like the SH ones, appear inside the folded zone rather than at the zone centre and the zone edges, and no straight lines are evident to link all gap positions. The small imaginary part of $k_{\mathrm{f}}$ for the coupled L and T phonons, shown in figure 2(d), allows one to observe more easily the positions of the gaps. These forbidden bands inside the folded Brillouin zone result from the so-called 'inter-mode Bragg reflection' [10, 24], which occur as a consequence of the mixing of different phonon modes [25] having a propagation direction oblique to the interfaces. For the SH phonons, enhanced reflection of them inside the gaps is expressed by $|\mathrm{Tr}[\mathbf{P}_{\mathrm{c}}]| > 2$, and the condition for the frequency pass bands by $|\mathrm{Tr}[\mathbf{P}_{\mathrm{c}}]| \leqslant 2$. When the SH phonons are the only ones, the extinction rule is satisfied for $|\mathrm{Tr}[\mathbf{P}_{\mathrm{c}}]| = 2$ when the reflection is totally suppressed [6]. For the coupled L and T phonons, these relations are no longer valid. From figure 2(b), $\mathrm{Tr}[\mathbf{P}_{\mathrm{LT}}]$ plotted against frequency, no evident connection can be observed between its behaviour and the band structures shown in figures 2(c) and (d) as opposed to the SH case where the limits of the bands correspond to $|\mathrm{Tr}[\mathbf{P}_{\mathrm{c}}]| = 2$. In an approximation assuming the constituent layers to be isotropic and non-piezoelectric, this intractable transfer matrix for the coupled L and T modes in the sagittal plane was first reduced to $4 \times 4$ and then approximated by an amenable $2 \times 2$ transfer matrix as far as the frequency gaps are concerned [26].

Figure 3 shows some Floquet slowness diagrams obtained using equation (10*d*) for the $(\bar{1}10)$ sagittal plane of GaAs/AlAs SL and at several frequencies. The results for homogeneous

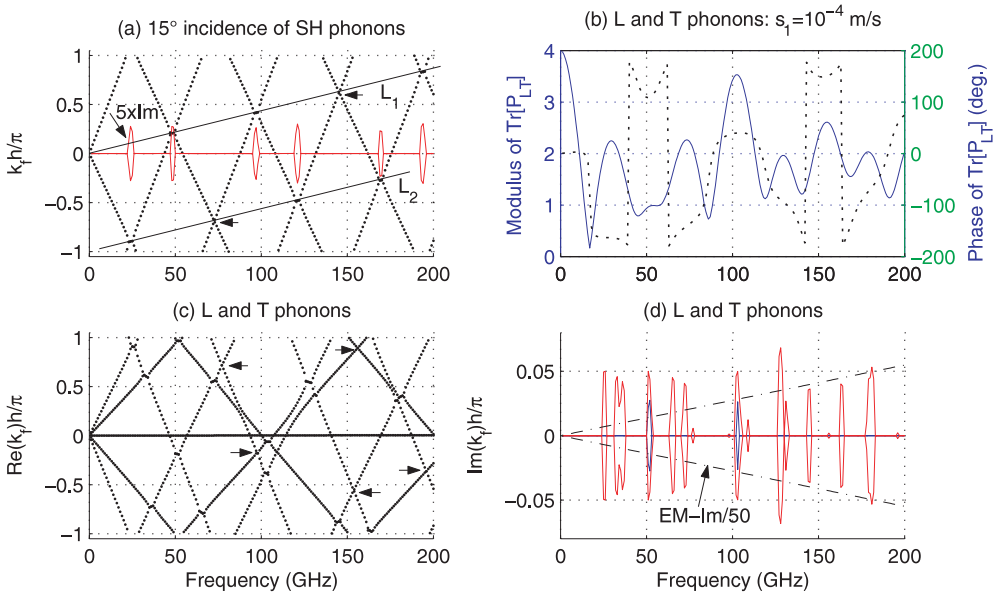


**Figure 2.** (a) Dispersion curves for a 15° incidence of SH phonons, red solid lines are imaginary part of the Floquet wavenumbers (inside stop bands), magnified five times. (b) Trace of the cell transfer matrix. (c) Real and (d) imaginary, parts of the Floquet wavenumbers for the coupled L and T phonons at $s_1 = 10^{-4}$ s m$^{-1}$, corresponding to an incidence of 32° for L and 18° for T modes. Note that the electromagnetic branches (black dot–dashed lines) are reduced 50 times, and the horizontal arrows in (a) and (c) indicate the positions of some very narrow gaps in which the reflection is insignificant.

bulk materials GaAs and AlAs are also given in figures 3(a) and (b) for comparison purposes. A Floquet slowness diagram consists of eight branches: two electromagnetic ones, which are always complex due to the adopted quasi-static approximation reducing the real part to the origin ($s_1 = s_f = 0$), and six acoustic ones, which may be either real or complex conjugate depending on the values of $s_1 = k_1/\omega$. Among acoustic branches, there are three types (L, T and SH polarized) of phonons, each type consists of an outgoing and an incoming mode. Outgoing (incoming) modes associated with a complex slowness $s_f$ decay (grow) exponentially along the positive $x_2$ direction normal to the layering. We observe from figure 3(c) that, at low frequencies (up to $f = 20$ GHz), acoustic branches remain real until at a sufficiently large $s_1$ the SL behaves like a homogeneous medium of some averaged constants with little dispersion. It is in this frequency range that the 'homogenization' idea applies [23, 27, 28]. For increasing values of $f$ above 30 GHz, the dispersion becomes more and more significant, as can be noted by comparing the patterns in figures 3(d)–(f). These results are compatible with those deduced from figures 2(a) and (c) where the dispersion curves $k_f(f)$ are seen, for $f \leqslant 20$ GHz, to be linear in frequency, meaning a constant velocity. Figures 3(d)–(f) also show that, for a fixed frequency, the dispersion sensitivity of a specific Floquet mode depends on $s_1$-values, i.e. incidence angles. The angles $\varphi$ of incidence ($m = 1$–4) and reflection ($m = 5$–8) are related to the $s_1$ value by $\tan\varphi^{(m)} = s_1/s_2^{(m)}$, $s_2^{(m)}$ being the bulk slowness of the relevant partial mode in the substrate. Floquet slowness diagrams are cuts in the dispersion surfaces along a plane and at a constant frequency. Their counterpart in 2D and 3D phononic crystals is called the 'equifrequency surface' [29–31] or 'constant frequency surface' [24]. Represented in the reduced zone scheme as in figure 3, they clearly show the evanescent modes which have

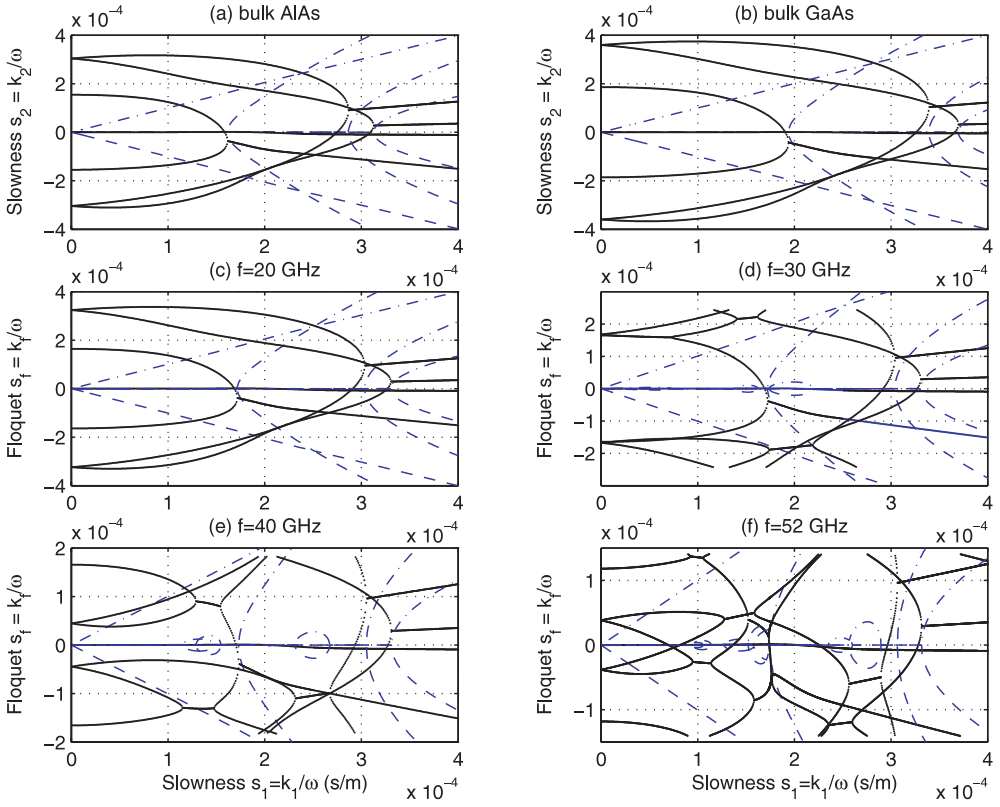


**Figure 3.** Floquet slowness diagrams for the $(\bar{1}10)$ plane of GaAs/AlAs SL: black solid lines are real parts and blue dashed lines are imaginary parts. Classical bulk waves in bulk GaAs (a) and AlAs (b). (c) At frequencies lower than the first stop band, a SL behaves like a homogeneous medium of somewhat averaged properties. (d)–(f) At higher frequencies, stop bands appear for certain $s_1$ values, indicated by $\mathrm{Im}(s_f) \neq 0$.

a non-zero imaginary part, and help identify the origin of a particular gap in relation to the dispersion curves in figure 2.

## 4. Transmission and reflection rates

Results obtained previously are rigorous only for a perfect (infinitely long and periodic) SL. For a finite SL sandwiched in between two homogeneous semi-infinite substrates, as depicted in figure 1, or a SL embedding one or more otherwise perfect foreign layers, Floquet theory is, strictly speaking, not valid, although it predicts approximate results if the number of layers is not too small. We now consider the transmission and reflection characters of a finite SL structure. The continuity of the state vector $\boldsymbol{\tau}$ at the interface separating the $(n+1)$th and $n$th layers is $\boldsymbol{\tau}_n^+ = \boldsymbol{\tau}_{n+1}^-$. Substituting in this relation their expressions from (5*a*) and (5*b*) leads to $\tilde{\mathbf{y}}_{n+1}^- = \mathbf{Q}_{n+1}^{-1}\mathbf{Q}_n\tilde{\mathbf{y}}_n^+$. With repetition of the above operation, we can get a relation between amplitudes in the substrate ($\mathbf{y}_S$) and in the detector ($\mathbf{y}_D$):

$$\tilde{\mathbf{y}}_D \equiv [\mathbf{a}]\tilde{\mathbf{y}}_S, \qquad \text{with } [\mathbf{a}] = \mathbf{Q}_D^{-1}\mathbf{P}_c^N\mathbf{Q}_S \tag{11}$$

where $N$ is the number of unit cells comprising the finite SL, and the subscripts D and S refer to the detector and substrate, respectively. The **a** matrix represents the finite SL transmission

matrix for the non-normalized amplitudes. It should be noted that the form of **a** using $\mathbf{P}_c^N$ is valid because all layers with even numbers are assumed to be of the same material, orientation and thickness, and so are the layers with odd numbers. Otherwise, the transfer matrix of the finite SL should be expressed as a cascading product of the individual transfer matrices. As mentioned in the previous section, the eight eigenmodes of a piezoelectric material are arranged into two groups of four modes each, namely the outgoing and incoming ones. In what follows, the eigenvalues and the associated eigenvectors of the phonons in the detector and substrate are assumed to have been arranged such that the outgoing (both propagating and decaying) modes in the $x_2$ direction are ordered in the first group, and the incoming ones follow.

The time-averaged acoustic energy flux associated with the lattice vibration of (1) is expressed in terms of the generalized Poynting vector as $p_j = -(1/2)\,\mathrm{Re}(^*\mathbf{v}\mathbf{T}_j)$, with **v** the generalized particle polarization velocity and $\mathbf{T}_j$ the stress components in the $x_j$-direction; thus $\mathbf{T}_2 = \tau(1{:}4)$. The left $*$ means the transposed complex conjugate. The $x_2$-directed power flow is obtained from

$$p_2 = -\,\mathrm{Re}(^*\mathbf{v}\mathbf{T}_2)/2 = \mathrm{Re}(^*\tilde{\mathbf{y}}\mathbf{P}\tilde{\mathbf{y}}) \tag{12}$$

with $\mathbf{P} \equiv -^*Q(5{:}8,:)Q(1{:}4,:)/2$, an eight-dimensional matrix. These expressions hold for both the detector and the substrate provided that the involved **Q** matrix is appropriate to the material layer in which $p_2$ is being considered. Thus the following unique expression is used for the power density of the phonons in both the detector (with subscript $x = \mathrm{D}$) and the substrate (with subscript $x = \mathrm{S}$) as

$$P_{2x} = \mathrm{Re}(^*\tilde{\mathbf{y}}_x\mathbf{P}_x\tilde{\mathbf{y}}_x) \tag{13}$$

with $\mathbf{P}_x \equiv -^*Q_x(5{:}8,:)Q_x(1{:}4,:)/2$. The amplitude $y_\mathrm{D}(5{:}8)$, which represents the reflected phonons in the detector layer, should vanish since no reflected phonons are assumed. This allows us to rewrite (13) for the detector as

$$p_{2\mathrm{D}} = \mathrm{Re}(^*\tilde{y}_\mathrm{D}(1{:}4)P_\mathrm{D}(1{:}4,\,1{:}4)\tilde{y}_\mathrm{D}(1{:}4)). \tag{14}$$

Introducing $\tilde{\mathbf{y}}_x^+ \equiv \tilde{y}_x(1{:}4)$ and $\tilde{\mathbf{y}}_x^- \equiv \tilde{y}_x(5{:}8)$ to shorten notations ($x = \mathrm{D}$ or S), and using the four sub-matrices of $\mathbf{P}_\mathrm{S}$, we can express $p_{2\mathrm{S}}$ from (13) for the substrate by the sum of four terms:

$$\begin{aligned} p_{2S} = \mathrm{Re}[&^*\tilde{\mathbf{y}}_S^+ P_\mathrm{S}(1{:}4,\,1{:}4)\tilde{\mathbf{y}}_\mathrm{S}^+ + {}^*\tilde{\mathbf{y}}_\mathrm{S}^- P_\mathrm{S}(5{:}8,\,5{:}8)\tilde{\mathbf{y}}_\mathrm{S}^- \\ &+ {}^*\tilde{\mathbf{y}}_\mathrm{S}^+ P_\mathrm{S}(1{:}4,\,5{:}8) + \tilde{\mathbf{y}}_\mathrm{S}^- + {}^*\tilde{\mathbf{y}}_\mathrm{S}^- P_\mathrm{S}(5{:}8,\,1{:}4)\tilde{\mathbf{y}}_\mathrm{S}^+]. \end{aligned} \tag{15}$$

The first term in the square brackets of (15) represents the energy flowing in the positive $x_2$ direction, due to the $x_2$-propagating phonons; the second one corresponds to the energy flowing in the negative $x_2$ direction due to the phonons reflected by the substrate–SL interface. The last two terms arise from the interaction between incident and reflected phonons.

Now, applying the orthogonality among the eight partial (eigen) modes, $\mathbf{Q}^{(m)}$ involved in the $\mathbf{P}_x$ matrix defined after (13), we were able to demonstrate that [21] the $\mathbf{P}_x$ matrix has the following properties: $^*\mathbf{P}_x = -\mathbf{P}_x$ when the eigenvectors $\mathbf{Q}^{(m)}$ ($m = 1$–8) are properly normalized. These properties allow us to write (14) as

$$p_{2\mathrm{D}} = \mathrm{Re}\sum_{m=1}^{4} P_\mathrm{D}(m,m)|\tilde{y}_\mathrm{D}(m)|^2. \tag{16}$$

Let $p_{2S}^+$ be the power density of the incident phonons in the substrate, and $p_{2S}^-$ that of the reflected ones. The same reasoning permits us to write (15) as

$$p_{2S} \equiv p_{2S}^+ + p_{2S}^-, \tag{17}$$

with

$$p_{2S}^{+} = \mathrm{Re}\sum_{m=1}^{4} P_{\mathrm{S}}(m,m)\,|\tilde{y}_{\mathrm{S}}(m)|^2 \tag{18a}$$

and

$$p_{\mathrm{S}}^{-} = \mathrm{Re}\sum_{m=5}^{8} P_{\mathrm{S}}(m,m)\,|\tilde{y}_{\mathrm{S}}(m)|^2\,. \tag{18b}$$

Moreover, it was also demonstrated that the diagonal elements corresponding to any bulk mode $m$ (i.e. for real $s_2^{(m)}$) are equal to $\pm 1$ provided that the eigenvector $\mathbf{Q}^{(m)}$ is normalized such that ${}^{*}\mathbf{Q}(5{:}8, m)\mathbf{Q}(1{:}4, m) = -(\pm 2)$ (here the upper sign refers to the incident modes and the lower one to the reflected modes). For the non-propagating modes, for which the value of $s_2^{(r)}$ is complex, the above normalization fails and the corresponding diagonal elements are identically zero, meaning that they contribute nothing to the phonon energies $p_{2\mathrm{D}}$ and $p_{2\mathrm{S}}$ [21]. For example, since the $s_2^{(1,8)}$ values are always complex, the powers associated with the electromagnetic modes are identically zero. If the incidence is due to the L phonons, then both the T and SH phonons are propagating for all incidence angles. If the incident phonons are of the slow shear mode, then the L and fast shear modes are not propagating so that the corresponding energies are null unless the incidence is close enough to the normal. When the fast shear phonons are incident, whether the L mode contributes depends on the incidence angle, but the slow shear mode does not, being propagating for all angles. The result is that those terms of $P_x(m,m)$ in (16) and (18) that are associated with complex $s_2^{(r)}$ can be removed from the summation.

We now relate the amplitudes of the incident and reflected phonons by defining some reflection and transmission matrices. Applying $\tilde{\mathbf{y}}_{\mathrm{D}}^{-} = \mathbf{0}$ in (11) leads to

$$\tilde{\mathbf{y}}_{\mathrm{S}}^{-} \equiv [\mathbf{r}]\tilde{\mathbf{y}}_{\mathrm{S}}^{+} \qquad \text{with } [\mathbf{r}] = -[a(5{:}8, 5{:}8)]^{-1}a(5{:}8, 1{:}4) \tag{19}$$

where $[\mathbf{r}]$ is the amplitude *reflection matrix*. Eliminating $\tilde{\mathbf{y}}_{\mathrm{S}}^{-}$ from (11) yields

$$\tilde{\mathbf{y}}_{\mathrm{D}}^{+} \equiv [\mathbf{t}]\tilde{\mathbf{y}}_{\mathrm{S}}^{+} \qquad \text{with } [\mathbf{t}] = a(1{:}4, 1{:}4) + a(1{:}4, 5{:}8)[\mathbf{r}] \tag{20}$$

where $[\mathbf{t}]$ is the amplitude *transmission matrix*. The power transmission ($T$) and reflection ($R$) rates are defined as the ratio of the squared amplitudes, i.e. given by

$$|\tilde{\mathbf{y}}_{\mathrm{S}}^{-}(n)|^2 \equiv R(n,m)|\tilde{\mathbf{y}}_{\mathrm{S}}^{+}(m)|^2 \qquad \text{with } R(n,m) = |t(n,m)|^2\,. \tag{21}$$

and

$$|\tilde{\mathbf{y}}_{\mathrm{D}}^{+}(n)|^2 \equiv T(n,m)|\tilde{\mathbf{y}}_{\mathrm{S}}^{+}(m)|^2 \qquad \text{with } T(n,m) = |t(n,m)|^2\,. \tag{22}$$

Equations (16)–(20) and the above stated properties of the $\mathbf{P}_x$ matrix have been accounted for in arriving at (21) and (22), with $n$, $m$ running over L, T, SH.

When the incident phonons come from the only SH mode ($m = 4$), one has $y_{\mathrm{S}}(4) \neq 0$ and $y_{\mathrm{S}}(1{:}3) = \mathbf{0}$. This can happen only if the SH is uncoupled with the other modes. Any incidence confined within the $(\bar{1}10)$ plane pertains to such a situation. In the same way, though the number of reflected modes is four in the most general case, mode uncoupling leads to $y_{\mathrm{S}}(5) \neq 0$ and $y_{\mathrm{S}}(6{:}8) = \mathbf{0}$. Similarly, for the transmitted phonons in the detector, the only non-null amplitude is $y_{\mathrm{D}}(4)$. Equations (14) and (15) for such a specific configuration reduces to

$$p_{2S} = |\tilde{y}_{\mathrm{D}}(4)|^2 \tag{23}$$

and

$$p_{2S} = |\tilde{y}_{\mathrm{S}}(4)|^2 + |\tilde{y}_{\mathrm{S}}(5)|^2. \tag{24}$$

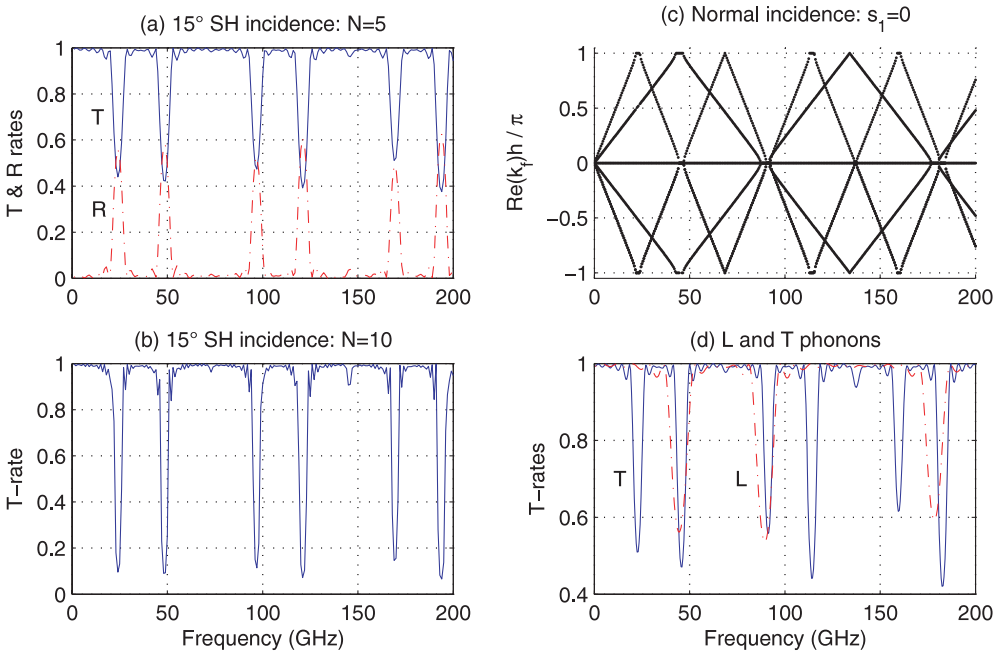


**Figure 4.** (a) Transmission ($T$) and reflection ($R$) rates of SH phonons in a finite SL with five unit cells ($N = 5$) and the same incidence angle as in figure 2(a). (b) $T$ rate obtained with $N = 10$. (c) Dispersion curves and (d) $T$ rates of the uncoupled L and T phonons at normal incidence with $N = 5$.

The $R$ rate of the SH phonons reflected by the SL is

$$R \equiv \frac{p_{2S}^{-}}{p_{2S}^{+}} = \frac{y_S(5)}{y_S(4)} = |r|^2 \tag{25a}$$

where $r$ is the amplitude reflection coefficient of the SH phonons and can be calculated from (19). The $T$ rate of the SH phonons from the substrate to the detector is

$$T \equiv \frac{p_{2D}}{p_{2S}^{+}} = \frac{y_D(4)}{y_S(4)} = |t|^2 \tag{25b}$$

where $t$ is the amplitude transmission coefficient of the SH phonons and can be calculated from (20). In the $(\bar{1}10)$ plane, however, if the incident phonons originate from an electrical excitation, both the L and T polarized phonons can always be transmitted and reflected but the SH is not concerned. The plane interface between layers imposes a coupling between the L and T modes. Their amplitudes are in effect related through (11). In other words, though $y_D(4) = 0$ when $y_S(4) = 0$, one cannot separately fix the amplitude of the L and T modes. When the incidence is out of the $(\bar{1}10)$ plane, all three modes, L, T and SH, will be coupled together.

## 5. Numerical results

*Transmission* ($T$) and *reflection* ($R$) rates of phonons in a SL structure were calculated for different values of the slowness $s_1$ and cell number $N$. The $R$ and $T$ rates of the SH phonons were calculated versus frequency by using equations (25*a*) and (25*b*). They are shown in figures 4(a) and (b), respectively, for $N = 5$ and 10 and assuming the same incidence angle

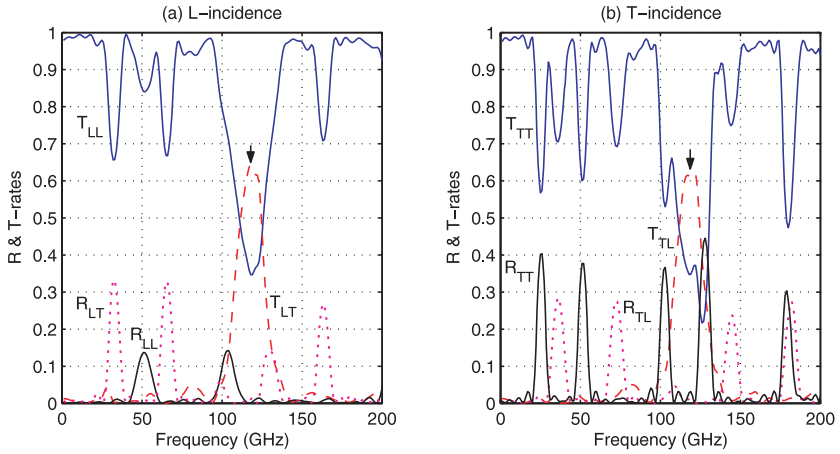


**Figure 5.** $T$ and $R$ rates of the coupled L and T phonons in a finite SL with $N = 5$. (a) L incidence, (b) T incidence with $s_1 = 10^{-4}$ s m$^{-1}$. Blue solid lines (at the top), L $\rightarrow$ L and T $\rightarrow$ T; red dashed lines, L $\leftrightarrow$ T transmission; black solid lines (at the bottom), L $\rightarrow$ L and T $\rightarrow$ T; magenta dotted lines, L $\leftrightarrow$ T reflection. The arrow indicates where a strong mode conversion occurs due to 'anti-crossing' between the L and T dispersion branches.

(15°) as in figure 2(a). We remark that $T + R = 1$ in figure 4(a) and the sum of the two rates of any intra-mode equals unity at any frequency. The very narrow stop bands (around 70 and 140 GHz, marked with an arrow in figure 2(a)) do not cause a noticeable dip or peak in the transmission and reflection spectra. In fact, these frequencies satisfy the extinction rules suppressing the reflection. The $T$ rate is much lowered (to about 0.1) in the stop bands when the cell number is doubled ($N = 10$ against 5). At normal incidence ($s_1 = 0$), both the SH and T phonons have the same velocity, and thus the same dispersion curves, and they are uncoupled from each other and from the L phonons. As seen from the dispersion curves plotted in figure 4(c) for the uncoupled L and S (shear) phonons, no gaps appear inside the Brillouin zone due to absence of the inter-mode coupling. The stop bands appear only at the centre ($k_\mathrm{f} = 0$) and edges ($k_\mathrm{f} h = \pm\pi$) of the folded Brillouin zones; this is because Floquet velocity of a mode remains unchanged when the propagation direction is inverted, as can be observed from figure 3 for $s_1 = 0$. The curves of the $T$ rates in figure 4(d) show more clearly that the width of a stop band and the distance between two neighbouring ones are larger for the L mode than for the S mode. The $R$ rates, not shown, were verified by taking (22) to be equal to $(1 - T)$ for both the L and S modes.

The $T$ and $R$ rates of the coupled L and T phonons at the same incidence as in figure 2(b) are plotted in figure 5 for $N = 5$ and in figure 6 for $N = 10$. We have plotted the $R$-rates in addition to the $T$ rates because their relationship is not as easily figured out as in figures 4(b) and (d). The $T$ rate of either L $\leftrightarrow$ L or T $\leftrightarrow$ T mode is close to unity except inside their respective gaps. The $T$ rates in figures 5 and 6 remain nearly unity in those narrow gaps, marked with a horizontal arrow in figure 2(c) and for which the imaginary part of $k_\mathrm{f}$ is negligibly small in figure 2(d). This implies that the reflection is insignificant in these gaps since these frequencies approximately satisfy the extinction rule. The transmission due to the mode conversion in figure 5 is generally rather small ($<0.05$) except around the frequency of about 120 GHz, marked with an arrow, where $T_{\mathrm{LT}}$ (T mode in the detector converted from incidence in the substrate of the L mode onto and through the SL) and $T_{\mathrm{TL}}$ (L mode in the detector due to T-mode incidence) take on a rather high value ($>0.6$). In the same range, $T_{\mathrm{LL}}$

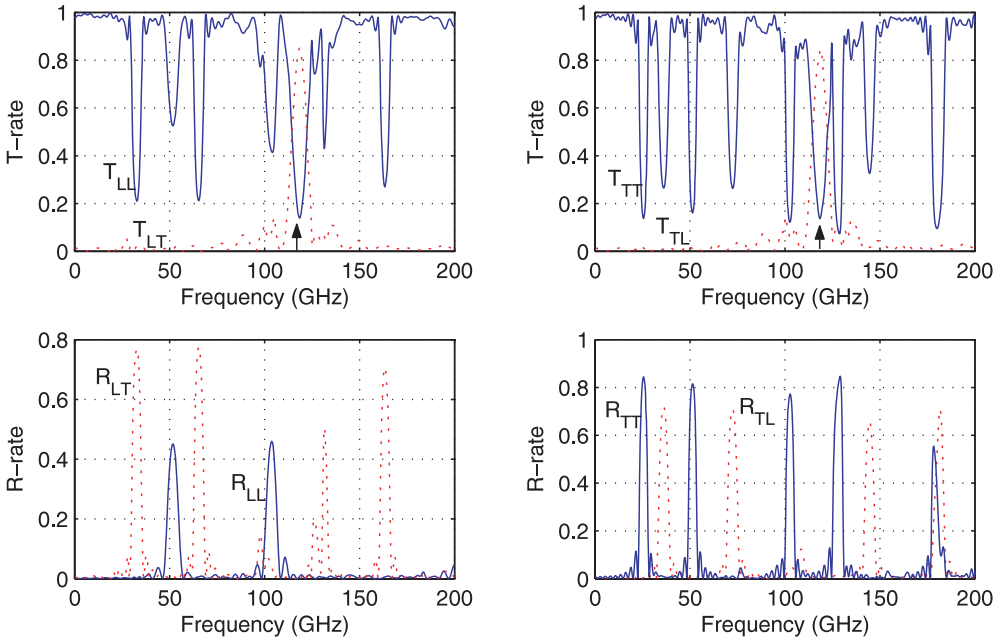


**Figure 6.** $T$ rate (top panel) and $R$ rate (bottom) of the coupled L and T phonons in a finite SL with $N = 10$ for an incidence of L (left panel) and T (right) phonons. The incidence angle is defined by $s_1 = 1.5 \times 10^{-4}$ s m$^{-1}$. Blue solid lines, L $\rightarrow$ L and T $\rightarrow$ T transmission and reflection; red dotted lines, L $\leftrightarrow$ T converted transmission and reflection. The arrow indicates where a strong mode conversion occurs due to 'anti-crossing' between the L and T dispersion branches.

and $T_{\mathrm{TT}}$ (transmitted modes keeping the same polarization) exhibit a noticeable dip. This occurs outside any frequency gap. Recall that the term 'gap' we use in this paper means a continuous frequency domain in which the wavenumber $k_{\mathrm{f}}$ is complex or at least pure imaginary. In fact, the phenomenon, as already remarked by Kato *et al* [5], is due to the 'anti-crossing' of the L and T branches of the dispersion curves in figure 2(c). It occurs for oblique incidence in SL structures and depends strongly on the SL length (number $N$). Our results confirm this observation, as seen from comparing figure 5 with the top panel of figure 6. For $N = 5$, there is a wide single lobe, which seems to split into three narrow ones on all transmission curves when the value of $N$ is doubled ($N = 10$). In the latter case, the SL reflection effects are much enhanced (by nearly 0.8 in most gap ranges) and the lobes become narrower. The conversion rate inside a gap and/or the anti-crossing zone will also strongly depend on the existence and the thickness of a foreign layer inserted into the structure, say at the entrance or the exit of the SL. By means of this property, it will become possible to control the mode conversion efficiency. It is also interesting to point out that not all dips in a transmission curve, $T_{\mathrm{LL}}$ at about 30, 50, and 65 GHz for example, are associated with the same physical phenomenon. Around 50 GHz, the dip of $T_{\mathrm{LL}}$ corresponds to a peak $R$ rate of the same polarization ($R_{\mathrm{LL}}$) with a negligible mode conversion in both the $T$ and $R$ rates ($T_{\mathrm{LT}}$ and $R_{\mathrm{LT}}$), while the other two dips of $T_{\mathrm{LL}}$ are associated with the peaks of $R$ of the different polarization ($R_{\mathrm{LT}}$), meaning a strong mode conversion around this frequency in the reflection spectrum. The same is true for the T incidence, with the three frequencies slightly shifted. Though the general features of the $T$ and $R$ curves in a gap display only slight modifications for $N$ varying from 5 to 10 unit cells, their dependence on the cell number $N$ is expected to be significant for $N$ larger than several

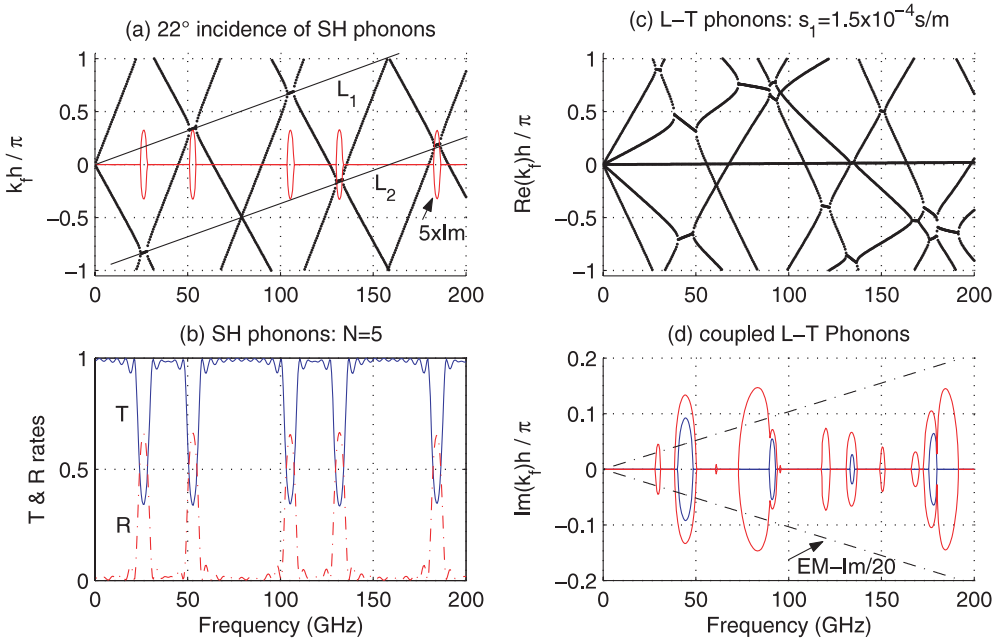


**Figure 7.** (a) Dispersion curves for a 22° incidence of SH phonons: red solid lines in closed ellipse form, imaginary part of $k_f$. (b) Corresponding $T$ and $R$ rates of SH phonons with $N = 5$. (c) Real and (d) imaginary, parts of $k_f$ for the coupled L and T phonons at $s_1 = 1.5 \times 10^{-4}$ s m$^{-1}$ corresponding to an incidence of respectively 53° for L and 30° for T modes. Note that the electromagnetic branches (black dot–dashed lines) are reduced 20 times.

tens in a GaAs/AlAs SL (inversely proportional to the impedance contrast). These behaviours can find an explanation from the dispersion curves displayed in figure 2(c), which show clearly the nature of a given gap among the three mentioned ones: the gap around 50 GHz is due to the intra-mode interaction, the other two are due to the inter-mode interaction. The dispersion spectra inherently do not repeat in a simple way with increasing frequency due to the incidence being oblique. The sum of the four curves in either figure 5(a) or 5(b) is equal to unity, as is required by energy conservation, and is numerically verified to be true. The same remark applies to the four curves in either the left or the right panel of figure 6.

The dispersion and transmission spectra of Floquet waves were also investigated as a function of incidence angle by considering different $s_1$ values. Results given in figures 7 and 8 were computed with $s_1 = 1.5 \times 10^{-4}$ s m$^{-1}$, which corresponds to a more oblique incidence (22°, 30°, and 53° for the SH, T, and L phonons, respectively). Comparing figure 7(a) with 2(a), we see that, for SH phonons, the width and separation of both gaps are a bit enlarged so that the last one goes out of the frequency range shown in the figure. Enlargement of the gaps is more noticeable for the coupled L and T phonons, as seen from figures 7(c) and (d). By comparing them with figures 2(c) and (d) we observe a more significant dispersion, with a larger magnitude of the imaginary part of the Floquet wavenumbers. The $T$ rates at this incidence are presented in figure 8 for $N = 5$. We observe that the mode-interaction becomes stronger with wider transmission dips for this more grazing incidence. Compared with figure 5, the top panel of figure 8 shows that both the width and position of the dips vary with incidence angle, and the transmission due to mode conversion stays at a low level, hardly exceeding 0.2 except around 100 and 180 GHz where it reaches 0.4. In the frequency ranges corresponding to the gaps in

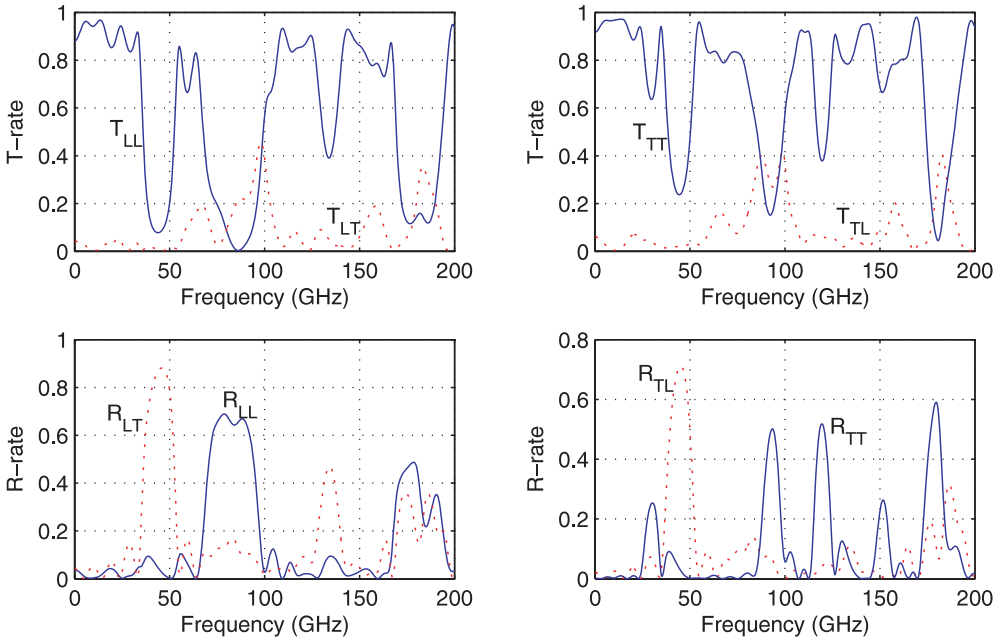


**Figure 8.** $T$ (top panel) and $R$ (bottom) rates of the coupled L and T phonons in a finite SL with $N = 5$ for an L (left panel) and a T (right) phonon incidence at an angle defined by $s_1 = 1.5 \times 10^{-4}$ s m$^{-1}$. The signification of curves labelling is the same as used in figure 6.

figures 7(c) and (d), the reflection is enhanced in general, the $R$ rate even reaches 0.9 in the band gap just below 50 GHz for L $\leftrightarrow$ T mode conversion. In addition, we remark that inside this range of frequencies all four transmission rates are very weak (<0.1). This is consistent with the dispersion curves displayed in figures 7(c) and (d) for the infinite SL, which clearly show the overlapping of the band gaps for both the L and T modes. Other similar gaps exist near 90, 130 and 175 GHz, but they still allow a significant transmission (>0.2) to take place for the converted mode. The phenomenon of inter-mode anti-crossing is not observed at this incidence. Results for $N = 10$, not shown here for lack of space, are rather similar except that the transmission dips and the reflection peaks are more pronounced: most of the $R$ rates exceed 0.8 and even reach an almost total reflection. It is worthwhile pointing out that for sufficiently grazing incidence ($s_1$ value approaching the bulk-threshold one, $s_c$), a T incidence cannot any longer give rise to the L phonons due to impossible mode conversion, and instead an interface mode can result from the lateral propagation along the layering at sufficiently high frequencies and for $s_1 > s_c$. Before ending, we recall that the dispersion curves in figures 2, 4(c), 7(a) and (c) are obtained assuming a perfect SL, i.e. the cell number $N \to \infty$, while the $R$ and $T$ curves are computed for some SLs of finite length.

## 6. Conclusions

In this paper, a theoretical model has been presented and semi-analytical expressions derived which allow the dispersion relations and the transmission ($T$) and reflection ($R$) properties of the coupled longitudinal and shear phonons to be numerically analysed. The unit cell transfer matrix $\mathbf{P}_c$ of the SL contains full information about the position and width of the stop

bands of Floquet modes in a perfect SL, and the $T$ and $R$ rates completely characterize the phonon motion in a SL of finite length or including some foreign layers with mode interactions accounted for. Closed-form expressions of the $T$ and $R$ rates are derived in terms of the modal and propagator matrices. All of these quantities are readily computable with little programming implementation effort. It suffices to resolve an eigenvalue problem (see (2)) by means of any available software, *MATLAB* for example for one to have numerically the modal and spectral matrices $\mathbf{Q}$ and $\mathbf{s}_2$ which then allow all calculations to be done straightforwardly. The state matrix of the associated ODE system has been given in terms of the material constants in addition to the parameter $s_1$ which refers to the incidence angle (see equation (3)). In the most general case as we have considered in this paper, no analytical results can be extracted from the unit cell transfer matrix which is algebraically much more complicated than its SH counterpart; the information it contains has to be numerically brought to light for the coupled phonon modes. The dependence of both the form and width of the phonons gaps on the cell number of the SL has also been investigated.

No absolute gaps were found in this SL configuration with the used parameters, due to the relatively narrow band gaps for both intra-mode and inter-mode interactions. There are two main physical reasons for this: one is the low impedance mismatch between the GaAs and AlAs materials, the other one is their weak piezoelectric coupling. However, the model established in this paper provides a powerful and general simulation tool allowing one to investigate SL made of materials with much higher impedance ratio (e.g. rubber and lead) or which are more strongly piezoelectric (AlN, GaN or PZT). In future works, it would be interesting to investigate how and to what extent the piezoelectric effects can affect the band structures of acoustic modes in a periodic 1D-SL or in higher-dimensional (2D and 3D) phononic crystals. This now becomes feasible using the results derived in the present paper. Application of the given model to analysing finite SL systems is straightforward, including SL with multilayer unit cells, double-barrier systems, multi-SL structures, semi-infinite SL as well as combinations of a finite SL with one (or two) semi-infinite homogeneous substrates which support surface (or interface) modes. New phenomena and effects are often associated with the defect modes resulting from local resonance of the complex systems. The presented model is expected to be useful in the design of SL-based filtering and de-multiplexing devices functioning either in the hypersonic tens of GHz range using acoustic phonons of nanometre structures or in sonic and ultrasonic frequency ranges using elastic-wave refraction phenomena such as focusing with a flat lens (negative refraction) and directional acoustic source by means of the defect mode cavity resonance (acoustic tunnelling).

## Appendix. Physical constants of (111)-oriented GaAs and AlAs materials

In the final $x_1x_2x_3$ system obtained by two consecutive rotations from the natural crystallographic axes $XYZ$ system, material constants tensors can be put into a single matrix

$$\begin{bmatrix} C_{11} & C_{12} & C_{13} & 0 & 0 & C_{16} & e_{11} & e_{21} & 0 \\ C_{12} & C_{22} & C_{12} & 0 & 0 & 0 & 0 & e_{22} & 0 \\ C_{13} & C_{12} & C_{11} & 0 & 0 & -C_{16} & -e_{11} & e_{21} & 0 \\ 0 & 0 & 0 & C_{44} & -C_{16} & 0 & 0 & 0 & e_{21} \\ 0 & 0 & 0 & -C_{16} & C_{55} & 0 & 0 & 0 & -e_{11} \\ C_{16} & 0 & -C_{16} & 0 & 0 & C_{44} & e_{21} & 0 & 0 \\ e_{11} & 0 & -e_{11} & 0 & 0 & e_{21} & \varepsilon_{11} & 0 & 0 \\ e_{21} & e_{22} & e_{21} & 0 & 0 & 0 & 0 & \varepsilon_{11} & 0 \\ 0 & 0 & 0 & e_{21} & -e_{11} & 0 & 0 & 0 & \varepsilon_{11} \end{bmatrix}.$$

With $x_2$ parallel to [111] and $x_1$ parallel to $[11\bar{2}]$, the values of the matrix elements for GaAs have been obtained as $C_{11} = 14.57$, $C_{12} = 3.587$, $C_{13} = 4.483$, $C_{16} = 1.268$, $C_{22} = 15.467$, $C_{44} = 4.147$, $C_{55} = 5.043$, $e_{11} = 0.1306$, $e_{21} = 0.0924$, $e_{22} = -0.1848$, $\varepsilon_{11} = 1.167$, $\rho = 5360\ \mathrm{kg\ m^{-3}}$; and those for AlAs as $C_{11} = 14.75$, $C_{12} = 3.880$, $C_{13} = 4.790$, $C_{16} = 1.287$, $C_{22} = 15.66$, $C_{44} = 4.070$, $C_{55} = 4.980$, $e_{11} = 0.1837$, $e_{21} = 0.1299$, $e_{22} = -0.2598$, $\varepsilon_{11} = 0.8907$, $\rho = 3760\ \mathrm{kg\ m^{-3}}$. In the above, the coefficients '$C$' are in units of $10^{10}\ \mathrm{N\ m^{-2}}$, '$e$' in $\mathrm{C\ m^{-2}}$ and '$\varepsilon$' in $10^{-10}\ \mathrm{F\ m^{-1}}$.

## References


[1] Camley R E, Djafari-Rouhani B, Dobrzynski L and Maradudin A A 1983 *Phys. Rev.* B **27** 7318
[2] Djafari-Rouhani B, Dobrzynski L, Duparc O H, Camley R E and Maradudin A A 1983 *Phys. Rev.* B **28** 1711
[3] Tamura S and Wolfe J P 1987 *Phys. Rev.* B **35** 2528
[4] Mizuno S and Tamura S I 1992 *Phys. Rev.* B **45** 734
[5] Kato H, Maris H J and Tamura S 1996 *Physica* B **219/220** 696
[6] Kato H 1997 *J. Acoust. Soc. Am.* **101** 1380
[7] Kato H and Tamura S 1997 *J. Phys.: Condens. Matter* **9** 6791
[8] Aono T and Tamura S I 1998 *Phys. Rev.* B **58** 4838
[9] Bria D, El Boudouti E H, Nougaoui A, Djafari-Rouhani B and Velasco V R 1999 *Phys. Rev.* B **60** 2505
[10] Mizuno S 2003 *Phys. Rev.* B **68** 193305
[11] Tamura S I, Watanabe H and Kawasaki T 2005 *Phys. Rev.* **72** 165306
[12] Hou Z, Fu X and Liu Y 2003 *Phys. Lett.* A **317** 127
[13] Wu T T, Huang Z G and Lin S 2004 *Phys. Rev.* B **69** 94301
[14] Wilm M, Khelif A, Ballandras S, Laude V and Djafari-Rouhani B 2003 *Phys. Rev.* E **67** 065602(R)
[15] Wu T T, Hsu Z C and Huang Z G 2005 *Phys. Rev.* B **71** 64303
[16] Zhang W, Liu Z and Wang Z 2005 *Phys. Rev.* B **71** 195114
[17] Zhang X, Liu Y, Zhu Y, Chen Y and Zhu S 2004 *Appl. Phys. Lett.* **85** 3531
[18] Huang C P and Zhu Y Y 2005 *Phys. Rev. Lett.* **94** 117401
[19] Adler E L 1990 *IEEE Trans. Ultrason. Ferroelectr. Freq. Control* **37** 485
[20] Zhang V Y, Lefebvre J E, Bruneel C and Gryba T 2001 *IEEE Trans. Ultrason. Ferroelectr. Freq. Control* **48** 1449
[21] Zhang Y, Desbois J and Boyer L 1992 *J. Acoust. Soc. Am.* **92** 2499
[22] Braga A M B and Herrmann G 1992 *J. Acoust. Soc. Am.* **91** 1211
[23] Potel C, de Belleval J F and Gargouri Y 1995 *J. Acoust. Soc. Am.* **97** 2815
[24] Imamura L and Tamura S 2004 *Phys. Rev.* B **70** 174308
[25] Nougaoui A and Djafari-Rouhani B 1987 *Surf. Sci.* **185** 154
[26] Imamura K, Tanaka Y and Tamura S 2002 *Phys. Rev.* B **65** 174301
[27] Wang L and Rokhlin S I 2002 *J. Acoust. Soc. Am.* **112** 38
[28] Ni Q and Cheng J 2005 *Phys. Rev.* B **72** 14305
[29] Kosaka H, Kawashima T, Tomita A, Notomi M, Tamamura T, Sato T and Kawakami S 1998 *Phys. Rev.* B **58** R10096
[30] Qiu C, Zhang X and Liu Z 2005 *Phys. Rev.* B **71** 54302
[31] Ke M, Liu Z, Qiu C, Wang W and Shi J 2005 *Phys. Rev.* B **72** 64306